Determination of the oxide scale growth mechanism using 18O-tracer experiments in combination with Transmission Electron Microscopy and nanoscale Secondary Ion Mass Spectrometry

Materials Characterization 136 (2018) 128–133

Contents lists available at ScienceDirect

Materials Characterization

journal homepage: www.elsevier.com/locate/matchar

Determination of the oxide scale growth mechanism using ^{18}O-tracer experiments in combination with Transmission Electron Microscopy and nanoscale Secondary Ion Mass Spectrometry

Hannes Falk-Windisch[a], Per Malmberg[b], Mohammad Sattari[a,1], Jan-Erik Svensson[a], Jan Froitzheim[a,*]

[a] Chalmers University of Technology, Department of Chemistry and Chemical Engineering, Division of Energy and Materials, Kemivägen 10, SE-41296 Gothenburg, Sweden
[b] Chalmers University of Technology, Department of Chemistry and Chemical Engineering, Division of Analytical Chemistry, Kemivägen 10, SE-41296 Gothenburg, Sweden

ABSTRACT

Two-stage $^{18}O_2/^{16}O_2$ exposures can be used to investigate the effect that alloying elements, secondary phases, or surface treatments have on the high temperature oxidation behaviour of certain materials. During subsequent exposures to $^{16}O_2$- and $^{18}O_2$-rich atmospheres, ^{16}O- and ^{18}O-rich layers are formed. Analysis of the layers using Secondary Ion Mass Spectrometry (SIMS) depth profiling allows for conclusions to be drawn about the oxide scale growth mechanism. The conclusions are, however, not entirely unambiguous due to the limited lateral resolution of the technology. Rough surface topography and the thickness variation of the oxide scale over the analysed volume add to the ambiguity of the findings. In this study, an Fe-20%Cr alloy was exposed to both ^{18}O- and ^{16}O-rich environments at 850 °C. Two methods were used to analyse the thermally grown Cr_2O_3 scale: (1) traditional SIMS depth profiling and (2) preparation of a cross-sectional lamellae for Transmission Electron Microscopy (TEM), which, subsequently, was analysed in a NanoSIMS. The NanoSIMS ^{16}O and ^{18}O elemental maps were then superimposed on the TEM image. In comparison with traditional SIMS depth profiling, the nanoSIMS elemental maps reveal detailed information about local oxide growth in different parts of an oxide scale. Moreover, a clear $^{16}O/^{18}O$ interface can be seen in the nanoSIMS maps, which is not the case in the sputter depth profiles. The findings of this study show that the aforementioned issues associated with sputter depth profiling can be eliminated by mapping a cross-section of an oxide scale using high resolution nanoSIMS.

1. Introduction

Two-stage $^{18}O_2$ and $^{16}O_2$, experiments, in combination with analytical methods, such as Secondary Ion Mass Spectrometry (SIMS), have been used for decades in high temperature corrosion studies with the aim to investigate the oxide scale growth mechanism of metals and alloys [1–5] as well as the effect that alloying elements, secondary phases, surface treatments, and coatings have on the growth mechanism of thermally grown oxide scales [5–20]. In a study by Quadakkers et al. [7], the corrosion resistance of both Cr_2O_3- and Al_2O_3-forming alloys with yttria oxide dispersions was compared to conventional wrought model alloys with similar compositions. By utilizing the oxygen isotope ^{18}O in a two-stage $^{18/16}O_2$ exposure, it was shown that the addition of yttria oxide dispersions suppresses scale growth by means of reduced cation outward diffusion, and that this change in growth mechanisms is a likely explanation for the observed decrease in scale growth and improved scale adherence for steels with yttria dispersions. Cotell et al. [6,10,11], used ^{18}O tracer experiments to study the effect ion implantation of yttrium (Y) has on the oxidation of pure chromium (Cr) in the temperature range 900–1025 °C. For the material with the highest dose of ion-implanted Y, Cr^{3+} flux was reduced to such an extent that the rate of O^{2-} transport was greater than that of Cr^{3+}, and, consequently, the predominant growth mechanism was changed from outward growth by means of cations to inward growth by means of oxygen ions as an effect of the Y ion implantation. Also Hussey and Graham [12], Papaiacovou et al. [9] as well as Chevalier et al. [13] have shown that coating an Fe-Cr alloy with a reactive element oxide coating can change the oxide scale growth mechanism from predominantly outward cation diffusion to predominantly inward anion diffusion. Thus, clear evidence of a change in the oxide scale growth mechanism has been observed in several studies. However, the findings have sometimes been ambiguous and conclusions somewhat

* Corresponding author.
E-mail addresses: hannes.windisch@chalmers.se (H. Falk-Windisch), jan.froitzheim@chalmers.se (J. Froitzheim).
[1] Currently at Chalmers University of Technology, Department of Physics, Division of Materials Microstructure, Fysikgränd 3, SE-41133 Gothenburg, Sweden.

https://doi.org/10.1016/j.matchar.2017.12.001
Received 10 July 2017; Received in revised form 29 November 2017; Accepted 1 December 2017
Available online 01 December 2017

speculative. Major sources of errors are the roughness of the oxide scale as well as uneven sputtering that creates a non-flat analysis area in the sputter crater [21]; this is a particular problem for thin oxide scales. A study by Fontana et al. [8] used ^{18}O tracer experiments to investigate the effect La_2O_3 and Y_2O_3 coatings have on the Fe-22Cr-0.5Mn steel Crofer 22 APU. A significant improvement in oxidation resistance was observed for the reactive element coated materials, however, the ^{18}O tracer experiments did not indicate a change in growth direction as was observed in other studies [9,10,13,22]. Moreover, Prescott et al. [23] used ^{18}O tracer experiments to study transport in α-Al_2O_3 scales on Fe-Al and Ni-Al alloys. It was shown that the scale growth process varied in different locations: either predominantly by means of metal outward diffusion or oxygen inward diffusion. Such local variations in the predominant growth direction may be very difficult to observe due to the often too large areas analysed using SIMS sputter depth profiling (lateral resolution often in the micron range or, in the best cases, a few hundreds of nanometres [24,25]). In the case of SNMS analysis, which is recommended for quantitative analysis, the lateral resolution is in the mm range [26]. Also Jedlinski et al. [27] concluded that only analytical methods that have respectable sensitivity and resolution can be used as a source of reliable information on the growth mechanisms of non-uniform, ridged scales. Since the area analysed often is in the micrometre range, it is important that the oxide scale grows homogenously. In order to form a more homogenous oxide scale, samples used for ^{18}O tracer experiments are often ground and polished before exposure. Surface treatment, such as grinding and polishing, may, however, influence oxidation behaviour [28–30]. The cited documents clearly show that ^{18}O-tracer experiments in combination with SIMS analysis is an effective method to gain fundamental knowledge about oxide scale growth mechanisms. Nevertheless, uneven oxide scales, non-uniform sputtering and limited lateral resolution of the SIMS depth profiling are some of the problems that have limited the use of ^{18}O tracer experiments in the field of high temperature corrosion. For this reason, the aim of this study is to develop a method that eliminates the obstacles associated with conventional SIMS sputter depth profiles.

2. Materials and Methods

2.1. Sample Preparation

For this study, an Fe-Cr model alloy with 20 wt% Cr, supplied by MaTeck (Jülich, Germany), was selected. 15 × 15 mm^2 samples were cut out, and for each sample a hole (2 mm in diameter) was drilled for hanging in the experimental setup. In order to have a flat surface before the exposure, the samples were ground and polished with SiC paper down to grit 4000. Subsequently the samples were cleaned for 10 min in acetone and ethanol using an ultrasonic bath. The exposures were carried out in a two-stage exposure setup. A schematic drawing of the experimental setup can be seen in Fig. 1. The samples were hung in a reaction chamber that was made of a quartz tube (with an inner diameter of 3.7 cm and a total length of 43 cm). In order to eliminate ^{16}O contamination during the ^{18}O exposure, the samples were exposed in a closed system. Temperature was controlled with a thermocouple located next to the samples. Before each exposure, the reaction chamber was evacuated down to 10^{-1} mbar. After the reaction chamber had been evacuated, the chamber was flushed with Argon. The reaction chamber was then, once more, evacuated before the exposure gases entered the reaction chamber. In this study, the Fe-20Cr model alloy was exposed for a total of 168 h and 500 h at 850 °C. The 168 h exposures was split into a first stage of 48 h Ar-20%$^{18}O_2$-$H_2{}^{18}O$ followed by 120 h in Ar-20%$^{16}O_2$-$H_2{}^{16}O$. The 500 h exposure was split into a first stage of 168 h Ar-20%^{18}O-$H_2{}^{18}O$ followed by 332 h in Ar-20%$^{16}O_2$-$H_2{}^{16}O$. The $^{18}O_2$ gas (98% ^{18}O compressed gas) was supplied by CK Isotopes, UK. The exposure times for the first stage were selected to achieve approximately half of the total oxide scale thickness when assuming parabolic type growth behaviour. The Ar-O_2 gas was humidified (~1%) to resemble ambient air conditions (the addition of water vapour is critical since humidification might influence the oxide scale growth mechanism for Fe-Cr alloys [31]). Approximately 1% moisture was achieved by bubbling half of the Argon gas through a glass capillary filled either with H_2O (distilled water) or $H_2{}^{18}O$ (Min. 98% ^{18}O enriched H_2O supplied by Rotem Industries Ltd., Israel) at room temperature. The total pressure in the reaction chamber, at room temperature, was 200 mbar. When switching the gas the reaction chamber was evacuated down to 10^{-1} mbar (without cooling down). After the reaction chamber had been evacuated, the evacuated chamber was flushed with dry argon before the chamber once again was evacuated down to 10^{-1} mbar before the exposure gases for the 2nd stage (^{16}O-rich atmosphere) was introduced into the reaction chamber. This process took less than 5 min.

To monitor the exposure atmosphere, a mass spectrometer (Pfeiffer Vacuum, PrismaPlus QMG) was coupled to the exposure chamber. The ratio between $^{16}O_2$ (mass 32 μ) and $^{18}O_2$ (mass 36 μ) as well as a mix of them $^{16,18}O_2$ (mass 34 μ) as a function of exposure time is shown in Fig. 2 for the 168 h exposure. A minor contribution of mass 36 signal is the ^{36}Ar isotope. However, the natural abundance of ^{36}Ar is sufficiently low to be neglected and no correction has been performed. Fig. 2 clearly shows that the concentration of $^{16,16}O_2$ during the first stage (0–48 h), and the concentration of $^{18,18}O_2$ during the second stage (48–168 h) was very low. A clear increase in $^{16,18}O_2$ can, however, be observed with time which is assume to be correlated to a surface exchange reaction during exposure. Nevertheless, Fig. 2 clearly proves that the sample was primarily exposed in an $^{18}O_2$-rich atmosphere during the first stage and in an $^{16}O_2$-rich atmosphere during the second stage.

2.2. Scanning transmission electron microscopy (STEM)

Lamellas for Transmission Electron Microscopy (TEM) were prepared using Focused Ion Beam (FIB) milling and lift-out technique in an FEI Versa 3D DualBeam instrument. Two layers of Pt, first with the help of an electron beam and, subsequently, with the help of an ion beam, were deposited on the surface of the sample in order to protect the region of interest from ion beam damage during milling. In order to reduce the amount of ion beam damage and amorphization, the samples were milled with a gradually decreasing beam current in the following sequence: 1000, 300, and 100 pA at 30 kV. For imaging, an FEI Titan 80–300 S/TEM microscope operated at an accelerating voltage of 300 kV was utilized.

2.3. Secondary Ion Mass Spectrometry (SIMS) Analysis

2.3.1. TOF-SIMS Depth Profiling

The SIMS depth profiles, shown in Fig. 4, were acquired using a TOF-SIMS V instrument (ION-TOF, GmbH, Münster, Germany) equipped with a 25 keV Bismuth LMIG (Liquid Metal Ion Gun) and a 10 keV Cs sputter gun that provided high precision information on the concentration of elements as a function of depth. Depth profiling and imaging was performed in the non-interlaced mode with 1 frame of analysis, 1 s of sputtering, and 0.5 s pausing per cycle while using the floodgun for charge compensation, while analysing an area of 25 × 25 μm and sputtering an area of 70 × 70 μm. The Bi-LMIG was set in collimated burst alignment mode [32] (mass resolution m/dm: 200; focus of the ion beam: 100 nm) using $Bi_1{}^+$ ions with a target DC current of 70 pA while Cs ions at 3 keV and a current of 0.3 nA were used for sputtering. Depth profile analyses were performed using the ION-TOF Surface Lab software (Version 6.3, ION-ToF, GmbH, Münster, Germany).

2.3.2. NanoSIMS on TEM Lamella

Oxygen isotope measurements were performed on the TEM cross section using a Cameca NanoSIMS 50L at the Chemical Imaging Infrastructure (CII) at Chalmers University of Technology and the

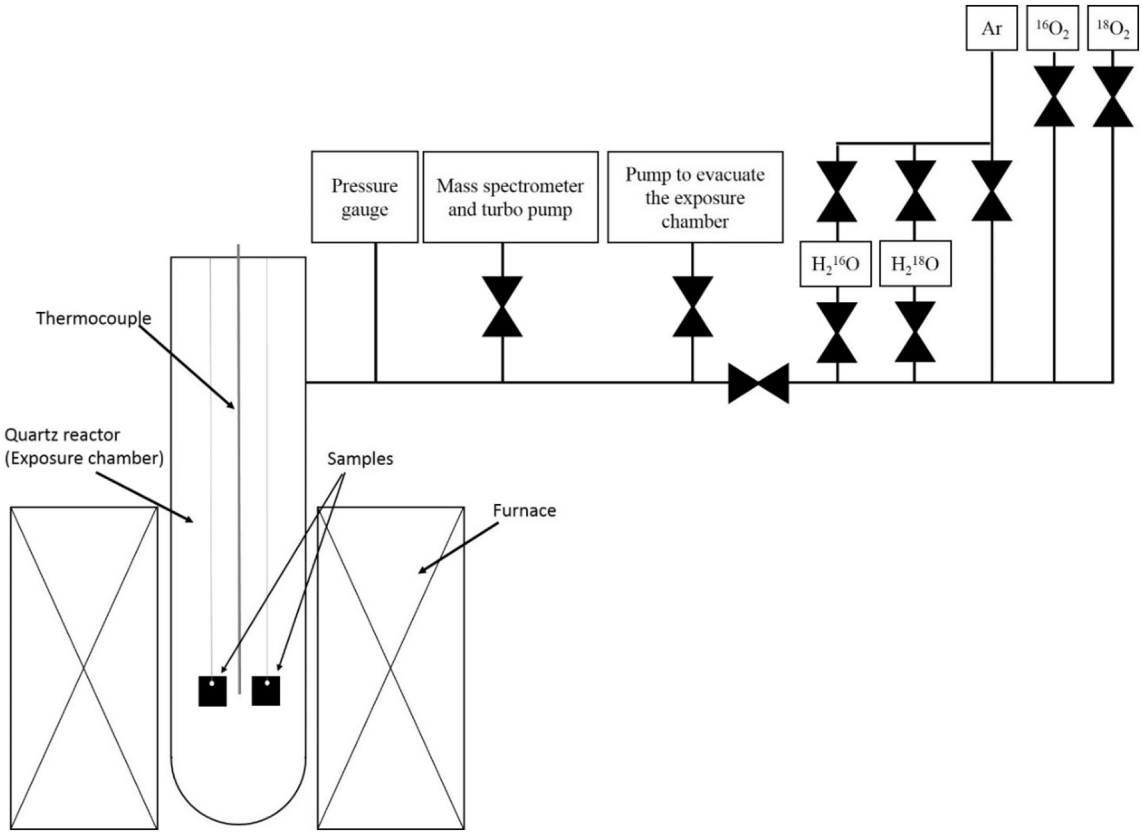

Fig. 1. Schematic drawing of the experimental setup.

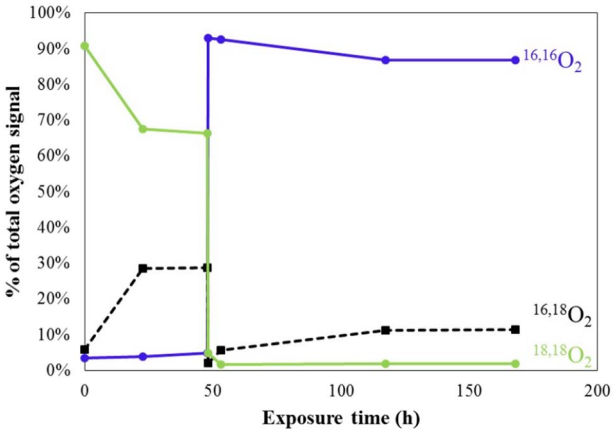

Fig. 2. Oxygen isotope concentration during the 168 h two-stage experiments. The concentration of the three oxygen molecules ($^{16,16}O_2$; $^{16,18}O_2$; and $^{18,18}O_2$) is based on the relative intensities from the masses 32, 34, and 36 μ.

University of Gothenburg. NanoSIMS images were acquired at 256 × 256 pixel resolution, and the field of views ranged from 8 × 8 μm to 10 × 10 μm. A medium primary ion beam aperture D1 = 3 was used to achieve high spatial resolution images of the oxide interface at approximately 50 nm spatial resolution [33]. ES3 was used to achieve sufficient mass resolving power (MRP) to avoid possible isobaric interferences. The OpenMIMS plugin (Harvard University) was used to process NanoSIMS images.

3. Results

The Cr_2O_3 scale formed on the model alloy after 168 h at 850 °C is approximately 1–2 μm in the TEM image in Fig. 3. The oxide grain size at the metal-oxide interface is very fine, in contrast to the crystals formed at the surface, which are almost in the μm-range.

In the TOF-SIMS sputter depth profiles in Fig. 4, it can be seen that the oxide scale formed during the second stage (^{16}O) is located at the surface of the Cr_2O_3 scale. Furthermore, it can be seen that the ^{16}O concentration levels off toward the metal-oxide interface. The oxide scale formed during the first stage (^{18}O) is, in contrast, located at the metal-oxide interface (assuming that the interface is located at the position where the total oxygen signal decreases) and decreases toward the surface of the sample.

Fig. 5 shows the ^{16}O and ^{18}O maps acquired using NanoSIMS on the TEM lamella from the 168 h sample (the same sample as in the TOF-SIMS depth profiles in Fig. 4). It can be seen in the figure that the oxide scale formed during the second exposure stage (^{16}O) is located at the gas-oxide interface, whereas the initial oxide scale formed during the first stage (^{18}O) is located at the metal-oxide interface. The ^{16}O and ^{18}O maps in Fig. 5 also show that local differences in oxide scale growth took place. In some areas, very little increase in oxide scale thickness is observed during the second stage (48–168 h) whereas, in other areas, large ^{16}O-rich grains were formed during the second exposure stage.

The data from the ^{16}O and ^{18}O maps in Fig. 5 can be used to plot line scans through the oxide scale (see Fig. 6). From these line scans, it can be seen that the area where the ^{16}O and the ^{18}O signals overlap is very small (100–300 nm), especially compared to the TOF-SIMS sputter depth profiles in Fig. 4. Furthermore, in Fig. 6 an ^{16}O-gradient can be observed within the ^{18}O-rich oxide layer. Such a gradient is not seen for the isotope ^{18}O within the ^{16}O-rich layer.

Fig. 7 shows the ^{16}O and ^{18}O maps acquired using NanoSIMS on a TEM lamella from the Fe20Cr sample that was exposed for 500 h. Similar to the results for the 168 h sample (Fig. 5) the oxide scale formed during the second exposure stage (^{16}O) is mainly located at the gas-oxide interface whereas the oxide scale formed during the first stage (^{18}O) is located at the metal-oxide interface. Compared to 168 h more

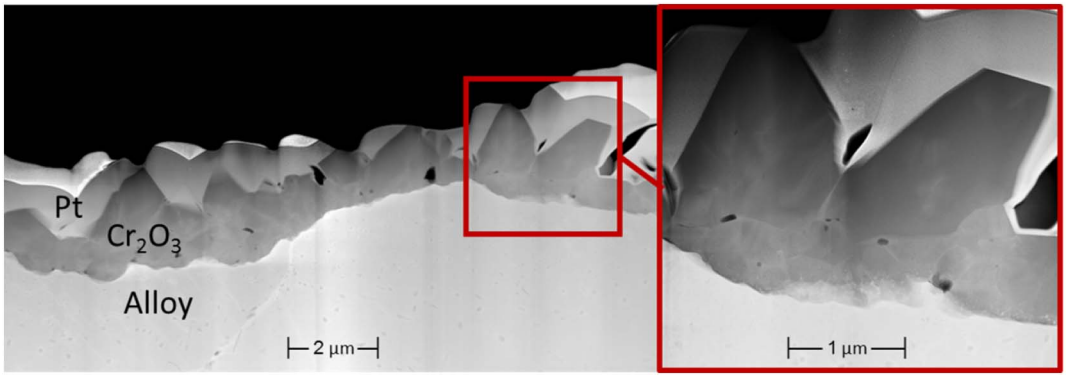

Fig. 3. High angle annular dark field (HAADF) Scanning transmission electron microscope (STEM) image of the Cr_2O_3 scale formed on the Fe20Cr alloy after 168 h (48 h in Ar-20% $^{18}O_2$ containing ~1% $H_2{}^{18}O$ + 120 h in Ar-20% $^{16}O_2$ containing ~1% $H_2{}^{16}O$) at 850 °C.

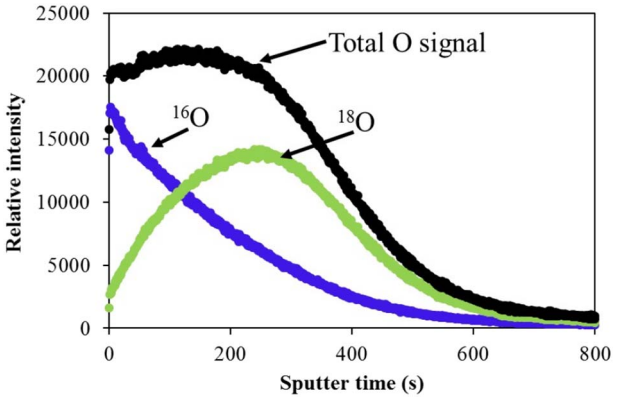

Fig. 4. TOF-SIMS depth profiles of the Fe20Cr model alloy after 168 h (48 h in Ar-20% $^{18}O_2$ containing ~1% $H_2{}^{18}O$ + 120 h in Ar-20% $^{16}O_2$ containing ~1% $H_2{}^{16}O$) at 850 °C. The intensity for ^{18}O (green), ^{16}O (blue), and ^{16}O plus ^{18}O (black) is plotted as a function of sputter time. (For the colour figure the reader is referred to the web version of this article.)

details of the oxygen isotope distribution within the oxide scale can be observed. Grain boundaries observed in the STEM image correlate well with ^{16}O-rich areas.

4. Discussion

Both the TOF-SIMS sputter depth profiles and the NanoSIMS maps from the TEM lamellas showed that the oxide scale is rich in ^{16}O at the gas-oxide interface and poor in ^{16}O at the metal-oxide interface. This indicates that the oxide layer, formed during the second stage (48–168 h and 168–500 h respectively), grew predominantly by means of outward cation diffusion. This is in good agreement with the literature where several studies have shown that thermally grown oxide scales formed on Fe-Cr alloys as well as other Cr_2O_3-forming alloys predominantly grow by outward diffusion of cations at elevated temperature [8,13,14,34]. However, for the hypothetical case of inward lattice diffusion of oxygen ions the TOF-SIMS profiles are expected to look very similar to the one in Fig. 4. This was schematically described by Reddy et al. [35]. In contrast, the NanoSIMS oxygen line scans and maps (Figs. 5 and 6) showed a clear interface between the ^{16}O- and the ^{18}O-rich oxide layers which clearly contradicts the interpretation of lattice diffusion of oxygen ions. The smeared out $^{16}O/^{18}O$ interface in the TOF SIMS depth profiles (Fig. 4) is due to a thin Cr_2O_3 scale (1–2 µm thick) and a rather rough surface in combination with large variations in scale thickness (see Fig. 3). With the high lateral resolution of the NanoSIMS this problem is eliminated. The advantage of this method is, however, not only to reduce or eliminate artefacts such as $^{16}O/^{18}O$ overlapping. The results presented in this work also show that additional information regarding the oxide scale growth mechanism can be obtained when TEM data is combined with NanoSIMS $^{16}O/^{18}O$ mapping. This becomes obvious in Fig. 7. The ^{16}O rich layer on the oxide surface provides evidence of oxide growth by metal cation diffusion as discussed above; moreover, areas identified as grain boundaries in the STEM image are enriched in ^{16}O. This matches well to an interpretation that undoped Cr_2O_3 grows by metal cation transport and oxygen inward transport (along grain boundaries). Although this has been speculated earlier, to the authors' knowledge, this is the first direct experimental evidence of oxygen transport along grain boundaries. Also for the 168 h sample oxygen ion inward diffusion along grain boundaries is believed to be part of the oxide scale growth mechanism. The line scans in Fig. 6 show that ^{16}O had diffused toward the metal-oxide interface forming an ^{16}O gradient within the ^{18}O-rich layer. Due to the much shorter diffusion time for the 168 h sample compared to the 500 h sample, the ^{16}O signal within the grain boundaries was most probably not high enough in order to be able to see ^{16}O-enrichment at the grain boundaries in the NanoSIMS map. It is predicted that the more detailed information gained by TEM/NanoSIMS will be very valuable in order to gain new insights into the oxidation mechanisms of the studied material.

5. Conclusions

In this study, an Fe20Cr model alloy was exposed for a total of 168 and 500 h in a two-stage $^{16/18}O$ exposure at 850 °C. The thermally grown Cr_2O_3 scale on the 168 h sample was analysed using two methods: (1) traditional TOF-SIMS depth profiling and (2) $^{16}O/^{18}O$ mapping of a cross section of the thermally grown Cr_2O_3 scale using high resolution NanoSIMS. Both techniques indicated that the dominant growth mechanism for the oxide layer was by means of chromium outward diffusion. This was very clear in the NanoSIMS maps. The NanoSIMS line scans and maps showed that a smaller part of the oxide scale growth is due to oxygen ion inward diffusion (mixed growth). Furthermore, the NanoSIMS maps also showed that there is strong local variation in oxide scale growth (individual grains grow differently). After 500 h the NanoSIMS map showed clearly that oxygen ions diffuse along grain boundaries toward the metal-oxide interface. The findings in this study show that much more reliable and detailed data can be generated from two-stage $^{16/18}O$ exposures by mapping a cross section of the sample using high resolution NanoSIMS than by using sputter depth profiles.

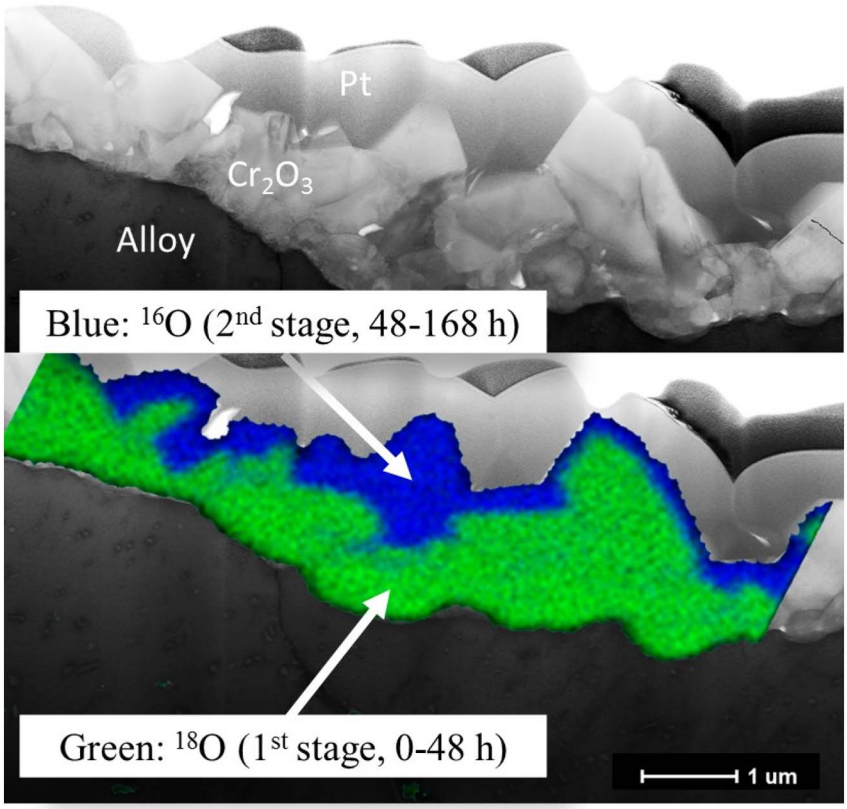

Fig. 5. ^{16}O and ^{18}O nanoSIMS maps of the TEM lamella shown in Fig. 3 that was prepared from the Fe20Cr model alloy exposed for 168 h (48 h in Ar-20% $^{18}O_2$ containing ~1% $H_2{}^{18}O$ + 120 h in Ar-20% $^{16}O_2$ containing ~1% $H_2{}^{16}O$) at 850 °C.

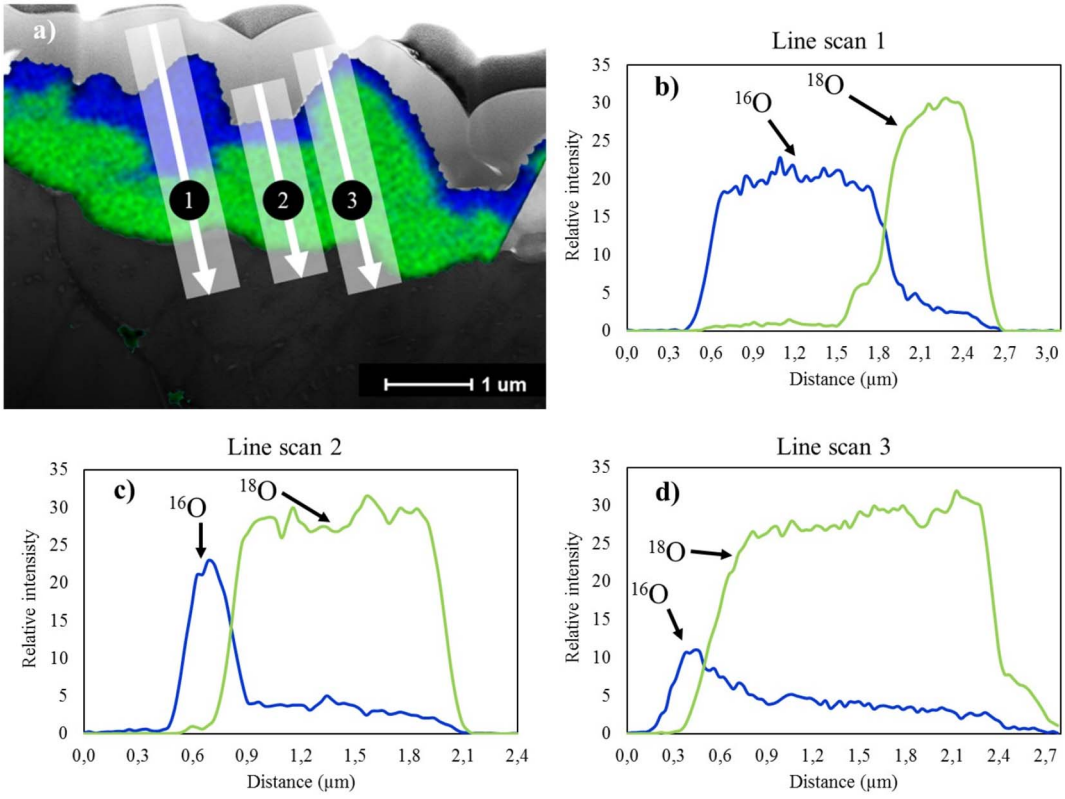

Fig. 6. NanoSIMS line scans (b, c, and d) at three different areas shown in a) of the Cr_2O_3 scale formed on the Fe20Cr model alloy exposed for 168 h (48 h in Ar-20% $^{18}O_2$ containing ~1% $H_2{}^{18}O$ + 120 h in Ar-20% $^{16}O_2$ containing ~1% $H_2{}^{16}O$) at 850 °C.

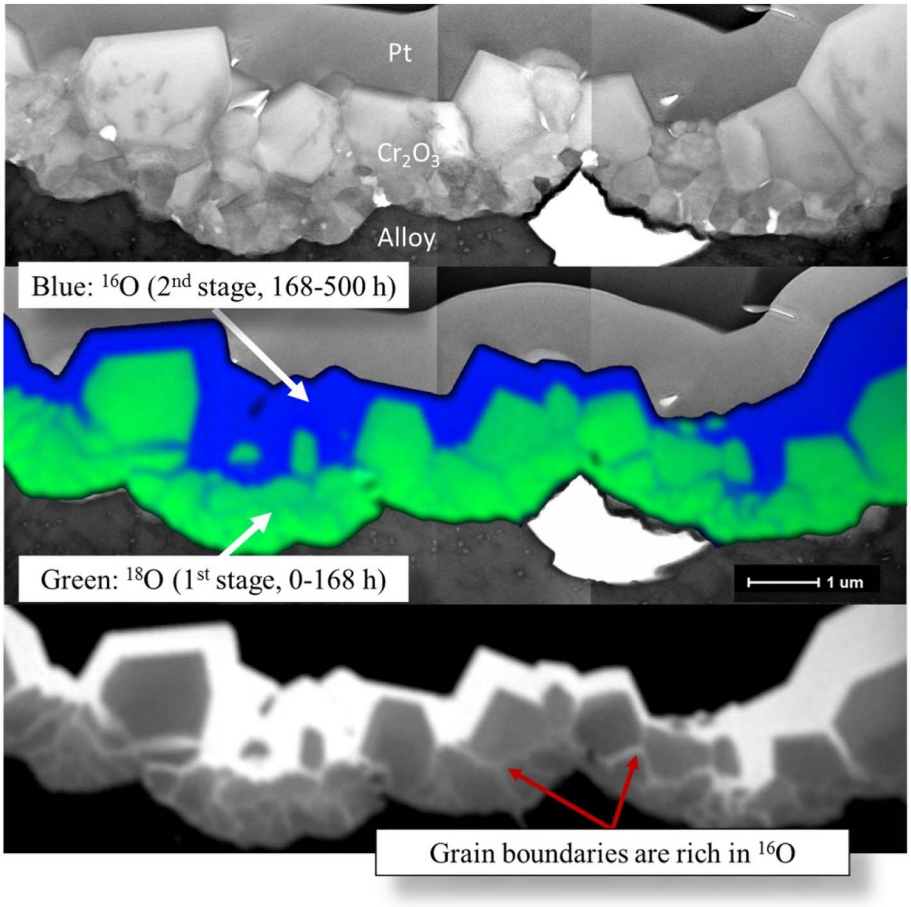

Fig. 7. ^{16}O and ^{18}O NanoSIMS map of the TEM lamella prepared from the Fe20Cr model alloy exposed for 500 h (168 h in Ar-20% $^{18}O_2$ containing ~1% $H_2{}^{18}O$ + 336 h in Ar-20% $^{16}O_2$ containing ~1% $H_2{}^{16}O$) at 850 °C. To better visualise the ^{16}O-enrichment within the grain boundaries an ^{16}O NanoSIMS map is shown in black and white underneath.

Acknowledgements

The research leading to these findings received funding from the Swedish Research Council and the Swedish Energy Agency, which are gratefully acknowledged. The NanoSIMS work was performed at the Infrastructure for chemical imaging at Chalmers University of Technology and University of Gothenburg. Professor Sebastien Chevalier (Université de Bourgogne-ESIREM) is also acknowledged for his advice when constructing the exposure setup and the fruitful discussions with respect to the ^{18}O tracer experiments.

References

[1] Y.P. Jacob, V.A.C. Haanappel, M.F. Stroosnijder, H. Buscail, P. Fielitz, G. Borchardt, Corros. Sci. 44 (2002) 2027–2039.
[2] S.C. Tsai, A.M. Huntz, C. Dolin, Oxid. Met. 43 (1995) 581–596.
[3] M. Skeldon, J.M. Calvert, D.G. Lees, Oxid. Met. 28 (1987) 109–125.
[4] M.J. Graham, Mater. High Temp. 17 (2000) 1–5.
[5] M.J. Graham, R.J. Hussey, Corros. Sci. 44 (2002) 319–330.
[6] C.M. Cotell, G.J. Yurek, R.J. Hussey, D.F. Mitchell, M.J. Graham, Oxid. Met. 34 (1990) 201–216.
[7] W.J. Quadakkers, H. Holzbrecher, K.G. Briefs, H. Beske, Oxid. Met. 32 (1989) 67–88.
[8] S. Fontana, S. Chevalier, G. Caboche, Oxid. Met. 78 (2012) 307–328.
[9] P. Papaiacovou, R.J. Hussey, D.F. Mitchell, M.J. Graham, Corros. Sci. 30 (1990) (451-&).
[10] C.M. Cotell, G.J. Yurek, R.J. Hussey, D.F. Mitchell, M.J. Graham, J. Electrochem. Soc. 134 (1987) 1871–1872.
[11] C.M. Cotell, G.J. Yurek, R.J. Hussey, D.F. Mitchell, M.J. Graham, Oxid. Met. 34 (1990) 173–200.
[12] R.J. Hussey, M.J. Graham, Oxid. Met. 45 (1996) 349–374.
[13] S. Chevalier, G. Bonnet, P. Fielitz, G. Strehl, S. Weber, G. Borchardt, J.C. Colson, J.P. Larpin, Mater. High Temp. 17 (2000) 247–255.
[14] S. Chevalier, G. Strehl, J. Favergeon, F. Desserrey, S. Weber, O. Heintz, G. Borchardt, J.P. Larpin, Mater. High Temp. 20 (2003) 253–259.
[15] S.C. Tsai, A.M. Huntz, C. Dolin, Mat. Sci. Eng. A-Struct. 212 (1996) 6–13.
[16] E.W.A. Young, J.H.W. Dewit, Oxid. Met. 26 (1986) 351–361.
[17] A.M. Huntz, Mater. Sci. Eng. 87 (1987) 251–260.
[18] B.A. Pint, J.R. Martin, L.W. Hobbs, Oxid. Met. 39 (1993) 167–195.
[19] C. Mennicke, E. Schumann, M. Ruhle, R.J. Hussey, G.I. Sproule, M.J. Graham, Oxid. Met. 49 (1998) 455–466.
[20] S. Chevalier, J.R. Larpin, R. Dufour, G. Strehl, G. Borchardt, K. Przybylski, S. Weber, H. Scherrer, Mater. High Temp. 20 (2003) 365–373.
[21] S. Hofmann, Rep. Prog. Phys. 61 (1998) 827–888.
[22] S. Chevalier, Mater. Corros. 65 (2014) 109–115.
[23] R. Prescott, D.F. Mitchell, G.I. Sproule, M.J. Graham, Solid State Ionics 53 (1992) 229–237.
[24] J. Hall, U. Bexell, J.S. Fletcher, S. Canovic, P. Malmberg, Mater. High Temp. 32 (2015) 133–141.
[25] T. Grehl, R. Mollers, E. Niehuis, Appl. Surf. Sci. 203 (2003) 277–280.
[26] H. Nickel, W.J. Quadakkers, L. Singheiser, Anal. Bioanal. Chem. 374 (2002) 581–587.
[27] J. Jedlinski, M.J. Graham, G.I. Sproule, D.F. Mitchell, G. Borchardt, A. Bernasik, Werkst. Korros. 46 (1995) 297–305.
[28] L. Cooper, S. Benhaddad, A. Wood, D.G. Ivey, J. Power Sources 184 (2008) 220–228.
[29] C. Ostwald, H.J. Grabke, Corros. Sci. 46 (2004) 1113–1127.
[30] J.T. Yuan, X.M. Wu, W. Wang, S.L. Zhu, F.H. Wang, Oxid. Met. 79 (2013) 541–551.
[31] S.R.J. Saunders, M. Monteiro, F. Rizzo, Prog. Mater. Sci. 53 (2008) 775–837.
[32] G. Holzlechner, M. Kubicek, H. Hutter, J. Fleig, J. Anal. Atom Spectrom. 28 (2013) 1080–1089.
[33] P. Hoppe, S. Cohen, A. Meibom, Geostand. Geoanal. Res. 37 (2013) 111–154.
[34] P. Huczkowski, N. Christiansen, S. V, L. Niewolak, J. Piron-Abellan, L. Singheiser, W.J. Quadakkers, Fuel Cells 6 (2006) 93–99.
[35] K.P.R. Reddy, J.L. Smialek, A.R. Cooper, Oxid. Met. 17 (1982) 429–449.